JGR Space Physics

RESEARCH ARTICLE
10.1029/2019JA027232

Special Section:
Equatorial Aeronomy: New results from the 15th International Symposium on Equatorial Aeronomy (ISEA-15) and beyond

All-Sky Imaging Observations of the Interaction Between the Brightness Wave and ESF Airglow Depletions

Dustin A. Hickey[1] **and Carlos R. Martinis**[2]

[1]National Research Council Postdoctoral Research Associate Resident at the U.S. Naval Research Laboratory, Washington, DC, USA, [2]Center for Space Physics, Boston University, Boston, MA, USA

Abstract The midnight temperature maximum (MTM) and equatorial spread F (ESF) are common processes in the low-latitude ionosphere and thermosphere. This work shows the first interaction between the brightness wave (BW), associated with the MTM, and plasma depletions, associated with ESF. Observations from the El Leoncito all-sky imager (ASI) (31.8°S, 69.3°W, 19.7°S magnetic latitude) show concurrent observations of a plasma depletion and a BW. As the BW passes through the depletion, the depletion is modified and becomes an enhancement. Concurrent measurements at the conjugate location show an airglow depletion, indicating that the enhancement is an evolution of the depletion and not a separate feature and that it only occurs in one hemisphere. Previous model results were able to recreate the evolution of an airglow depletion into an enhancement when there is a poleward wind combined with converging zonal winds. We discuss how these wind conditions are often associated with the MTM/BW and can explain this observed enhancement.

Key Points:
- Presented here is the first observation of an interaction between a BW and an ESF depletion
- ESF depletion evolves into an enhancement in only one hemisphere as the BW passes by
- Evolution of the ESF structure is attributed to neutral winds associated with the MTM/BW

Supporting Information:
- Supporting Information S1
- Movie S1
- Movie S2
- Movie S3
- Movie S4

Correspondence to:
D. A. Hickey,
dustin.hickey.ctr@nrl.navy.mil

Citation:
Hickey, D. A., & Martinis, C. (2020). All-sky imaging observations of the interaction between the brightness wave and ESF airglow depletions. *Journal of Geophysical Research: Space Physics*, *125*, e2019JA027232. https://doi.org/10.1029/2019JA027232

Received 30 JUL 2019
Accepted 27 FEB 2020
Accepted article online 16 APR 2020

1. Introduction

Two separate but common processes that occur in the Earth's upper atmosphere at low latitudes are the midnight temperature maximum (MTM) and equatorial spread F (ESF). The MTM is an increase of about 50 to 200 K in neutral temperature in the upper atmosphere that creates a local maximum in the temperature near local midnight. The formation mechanism for the MTM is not fully understood but results from the Whole Atmosphere Model (WAM) indicate that the generation of the MTM may be largely due to effects from an upward propagating terdiurnal tidal wave in addition to other, smaller, nonlinear interaction effects (Akmaev et al., 2009). Recent observations of the MTM and its effects support this explanation (e.g., Hickey et al., 2014, 2018).

The temperature increase of the MTM creates a pressure bulge in the thermosphere. This pressure bulge drives winds away from the MTM, and these thermospheric winds drag the ions with them. In particular, the MTM can change the meridional wind by decreasing or even reversing the normally equatorward direction (Meriwether et al., 2008). As the wind drags the plasma, the plasma moves down along magnetic field lines increasing the brightness in airglow observations. Observations of this brightness wave (BW), an optical signature of the MTM (Colerico et al., 1996), by all-sky imagers (ASIs) have been used as evidence of the MTM occurring at midlatitudes in the Southern Hemisphere. These optical signatures in airglow emissions at 6300 Å have been observed as far as 40°S (Colerico et al., 2006). Additionally, the brightness wave and associated winds have been observed in other longitude regions as well (Otsuka et al., 2003). The brightness increase is a result of the ions in the ionosphere, driven by neutral winds associated with the MTM (Colerico et al., 1996, 2006), moving down to a lower altitude. At a lower altitude, there are more collisions that excite oxygen to the state need to emit a photon at 6,300 Å. In the southern hemisphere, the BW moves south as the ions move down in altitude along the magnetic field lines. In the northern hemisphere, the ions that are moving northward also move down in altitude and increase the emission. The MTM is moving westward during this time, and the net result in the southern hemisphere is a wave of brightness that propagates southwestward across the image. In the northern hemisphere, it propagates northwestward.

The other low latitude process discussed in this paper is ESF, the name commonly given to plasma irregularities that typically occur after sunset in the equatorial and low-latitude F region. These irregularities are attributed to plasma bubbles, depletions in the background plasma that begin to form due to the generalized Rayleigh-Taylor instability (Hysell, 2000). Large-scale ESF structures, with longitudinal widths that can be

tens to hundreds of kilometers, can be observed as airglow depletions within the field of view of ASIs (Weber et al., 1978). These structures are regions that have less plasma and thus are darker than the background. Depletions can be associated with three types of ESF: bottom-type, bottomside, and topside (Woodman & La Hoz, 1976). At the magnetic equator, we observe bottomside ESF, and these structures appear as dark bands oriented along magnetic field lines. Observations away from the magnetic equator measure topside ESF and are visible as finger-like structures extending away from the magnetic equator and are sometimes bifurcated. ESF processes are flux tube integrated (e.g., Keskinen et al., 1998; Sultan, 1996; Weber et al., 1996) so the topside structures at the magnetic equator map down to their magnetic foot points at higher latitudes (e.g., Mendillo & Baumgardner, 1982). Including northern and southern hemisphere coupling in simulations of ESF development produces a more accurate development of plasma bubbles (Keskinen et al., 1998). The flux tube that contains the plasma bubble has low density all along the magnetic field lines from one hemisphere to the other. These depleted flux tubes can be observed in airglow with ASIs in both hemispheres (Hickey et al., 2018; Martinis et al., 2018)

The MTM and ESF have some similarities in occurrence time and location. They both occur in the same altitude region of the upper atmosphere, typically occur in the same latitude range, and are nighttime events. ESF occurs mostly during postsunset and the MTM occurs around midnight so simultaneous observations are infrequent. The overlap of regions with ESF and the MTM can be observed readily with an ASI at latitudes between about 10° and 30° from the magnetic equator. At these latitudes, the effect of the MTM is observed as a brightness wave (BW) in the ASI field of view as there is a downward motion of the plasma. Airglow depletions at these latitudes are associated with ESF structures that map to the topside of the ionosphere at the magnetic equator. The brightness wave can occur during the same time period that ESF occurs, but this does not happen very often.

This paper presents a case where the BW associated with the MTM alters the characteristics of plasma depletions associated with ESF.

2. Data

The main sources of data for this paper are ASIs. Boston University operates a network of a ASIs around the world (Martinis et al., 2018). This work focuses on ASIs located in South America. One ASI is located in El Leoncito, Argentina (31.8°S, 69.3°W, 19.7°S magnetic latitude) and has been operating there since 1999. The other ASI is located in Villa de Leyva, Colombia (5.6°N, 73.52°W, 16.2°N magnetic latitude) and was installed in October 2014. Figure 1 shows the location and fields of views of the ASIs that are used in this study. The dots indicate the locations of the ASIs and the circles are the field of view of the imagers at 250 km and a zenith angle of 80°. The two imagers are located such that they are very close to being on the same magnetic field line of the Earth. The field of view of each imager includes the magnetic conjugate point of the other imager, indicated by triangles in Figure 1. The blue lines are lines of constant magnetic apex altitude and the magnetic equator is marked by a blue dashed line.

Both ASIs have a filter wheel that cycles through five filters (5,577 Å, 6,950 Å, 7,774 Å, 6,300 Å, and 6,050 Å). The El Leoncito ASI also has an additional filter at 5,893 Å. The cadence between images with the same filter is about 9 min at El Leoncito and 7 min at Villa de Leyva. The 6,050 Å is used for calibration purposes and the rest of the filters are used to observe different processes in the mesosphere and thermosphere. This work focuses on 6,300 Å and 7,774 Å observations, which are both related to electron density in the ionosphere. Production of 6,300 Å is multistep process involving oxygen. The first step is charge exchange between molecular oxygen and ionized atomic oxygen. When the ionized molecular oxygen recombines, it dissociates and creates an excited neutral atomic oxygen in the ^1D state. The excited oxygen can deexcite by quenching with neutrals or by the spontaneous emission of a 6,300 Å photon. The conditions for this to occur are met in the bottomside of the F region of the ionosphere. Emission is limited to a small altitude range (about 50 km) that is typically centered near 250 km but varies and can be as high as 400 km early in the night. The emission is proportional to the plasma density, the altitude of ionosphere, and the neutral density. For a more detailed analysis of 6,300 Å emission, see Colerico et al. (2006). 7,774 Å emission is caused by the radiative recombination of O^+ and is directly proportional to the square of the electron density. The peak emission of 7,774 Å is usually at the same altitude of the peak of the F region, 300 to 350 km.

In addition to the ASI observations, total electron content (TEC) from Global Positioning System (GPS) receivers are used to further investigate the BW. These data come from the MIT Automated Processing of

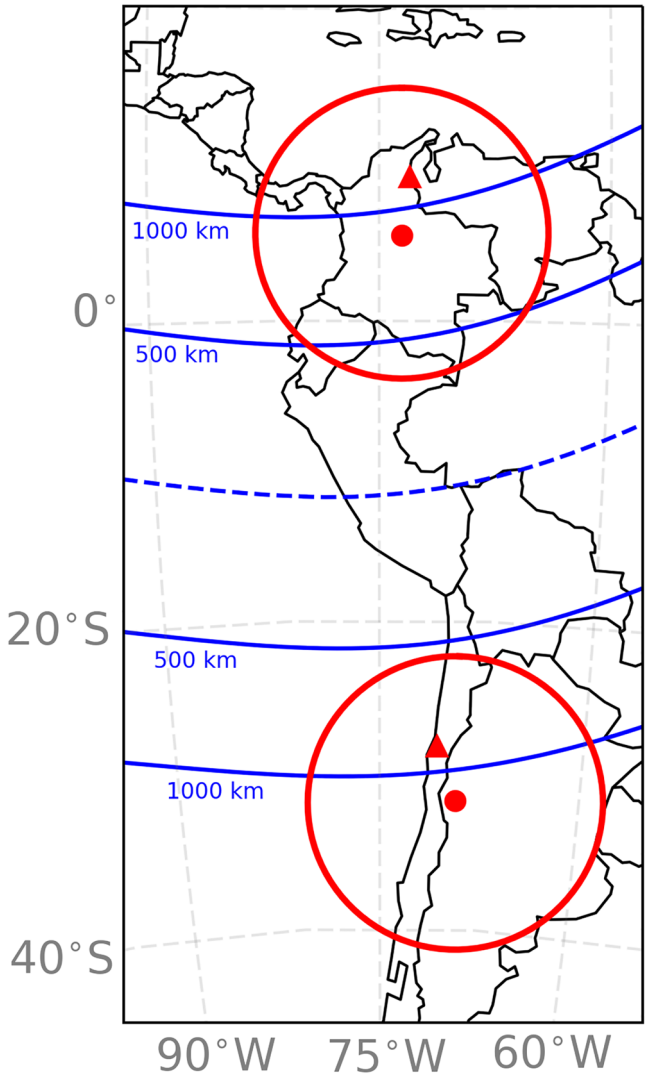

Figure 1. A map of western South America showing the locations of the ASIs used in this study. The dots indicate the locations of the ASIs and the the circles are the field of view of the imagers at 250 km. The magnetic conjugate location of each imager is marked by a triangle. The more northern ASI is the Villa de Leyva ASI in Colombia and the more southern ASI is the El Leoncito ASI in Argentina.

GPS (MAPGPS) on the Madrigal website (Rideout & Coster, 2006; Vierinen et al., 2015). The data outputs are vertical TEC in 1° by 1° bins and 5 min increments.

3. Analysis

From the 20 years of observations at El Leoncito, we examined 5 years in detail to look for cases when the BW and ESF structures appear at the same time and found few cases, mostly due to the fact that ESF occurs early in the night and the BW occurs late in the night. Numerous observational and modeling studies have examined how the MTM timing varies with latitude (e.g., Akmaev et al., 2010; Herrero & Spencer, 1982; Hickey et al., 2014). These studies have all found that the MTM occurs later at higher geographic latitudes. As a result, the BW mostly occurs at El Leoncito after local midnight, sometimes near predawn hours. The recent work by Hickey et al. (2018) analyzed the timing of a BW at El Leoncito and an MTM observed at Jicamarca on 4 April 2014. The observations in that work supported the idea that, spatially, the MTM has a sideways V structure, and this structure moves westward with the apparent motion of the sun. In contrast to the MTM, ESF most often forms just after sunset when the prereversal enhancement of the electric field causes a large upward drift near the magnetic equator (e.g., Fejer et al., 1999). This means that most ESF

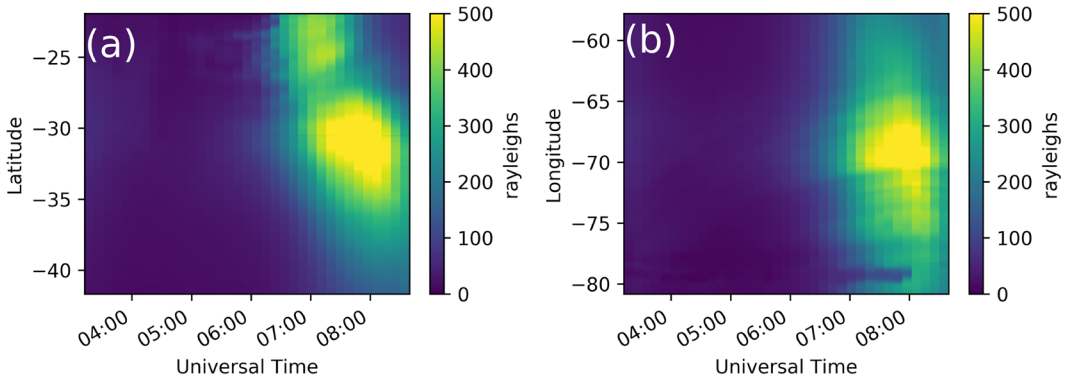

Figure 2. Two plots showing measurements of the BW throughout the night on 29 October 2014. The plots were made from images unwarped at 280 km. (a) On the left is a color plot showing the brightness in rayleighs at the center longitude of the image at each latitude. The vertical axis is latitude, and the horizontal axis is time. (b) The right plot is similar to the left except it is at a constant latitude at the center of the image and shows all longitudes.

depletions observed at El Leoncito occur early in the night. There are two ways for ESF to be present later in the night (postmidnight). The depletions can be formed later in the night or the early depletions can persist throughout the night. Post midnight ESF can be produced by geomagnetic storms (e.g., Kelley & Maruyama, 1992; Martinis et al., 2005) or by an ionospheric upwelling during quiet times (Rodrigues et al., 2018; Zhan et al., 2018). Early depletions that persist have stopped growing and are referred to as fossil depletions (Krall et al., 2010). Thus, it is possible to have depletions appearing in the ASI images at the same time that the BW passes through the field of view.

On 29 October 2014, a BW was observed at El Leoncito moving from the northeast to the southwest. Figure 2 shows keograms in longitude and latitude that show the BW as the increase in brightness toward the end of the night. These keograms show the brightness at a constant longitude at all latitudes (a) and at a constant latitude at all longitudes (b). The all-sky images were unwarped at an altitude of 280 km. This altitude was calculated using ionospheric profiles from the International Reference Ionosphere (IRI-2016) (Bilitza et al., 2017) and thermospheric profiles from the Naval Research Laboratory Mass Spectrometer Incoherent Scatter Radar model that extends to the exobase (NRLMSISE-00) (Picone et al., 2002) on this date. The equation for this calculation is found in Colerico et al. (2006). In Figure 2a, it can be seen that the BW is moving south as time goes on. The decrease in brightness around 28°S is due to the presence of ESF depletions on this night. Figure 2b shows a faster westward motion compared to the southward motion, as seen by the steeper slope of the BW. We estimate the meridional and zonal velocities of the BW on this night by tracking the center of the BW in the keograms. There are large errors associated with determining these velocities due to the extended nature of the BW. We found that the zonal velocity is about 450 m/s westward and the meridional velocity is about 300 m/s southward. Included in the Supporting Information is a movie from the ASI images showing the BW in 6,300 Å. Additionally, a movie at 7,774 Å is included. This emission shows a brightness increase that precedes the 6,300 Å emission. The 7,774 Å increase is discussed later in the context of TEC variation.

The data presented in Figure 2 are from a date when both a BW and ESF are observed at the same time but no interaction takes place, meaning that the brightness of the airglow depletions remains unaltered after the passage of the BW. Figure 3 shows four all-sky images from this night (top) and a plot of the brightness at zenith around the time of the BW (bottom). The first image at 06:47 UT shows airglow depletions and the initial stage of the BW and the last image at 08:39 UT shows how the depletion moved eastward and the BW moved south past zenith. The plot on the bottom shows the intensity of 6,300 Å emission calculated as the average from 10×10 pixel box at zenith as a function of time. The standard deviation of the mean is included as error bars on the plot but are mostly smaller than the points. Four vertical dashed lines mark the times of the images. The peak around 08:00 UT indicates the presence of brightness wave. The ESF structure is visible as the dark feature extending from the top of the images down toward the bottom. As the background emission increases, the morphology and brightness of the ESF depletions do not change.

Figure 4 shows a case from 13 May 2015 when both a BW and an ESF depletion are observed, but with a different outcome than on 29 October 2014. The images are unwarped at an altitude of 250 km. This differs from 29 October 2014 because the outputs for IRI-2016 and NRLMSISE-00 are slightly different for this

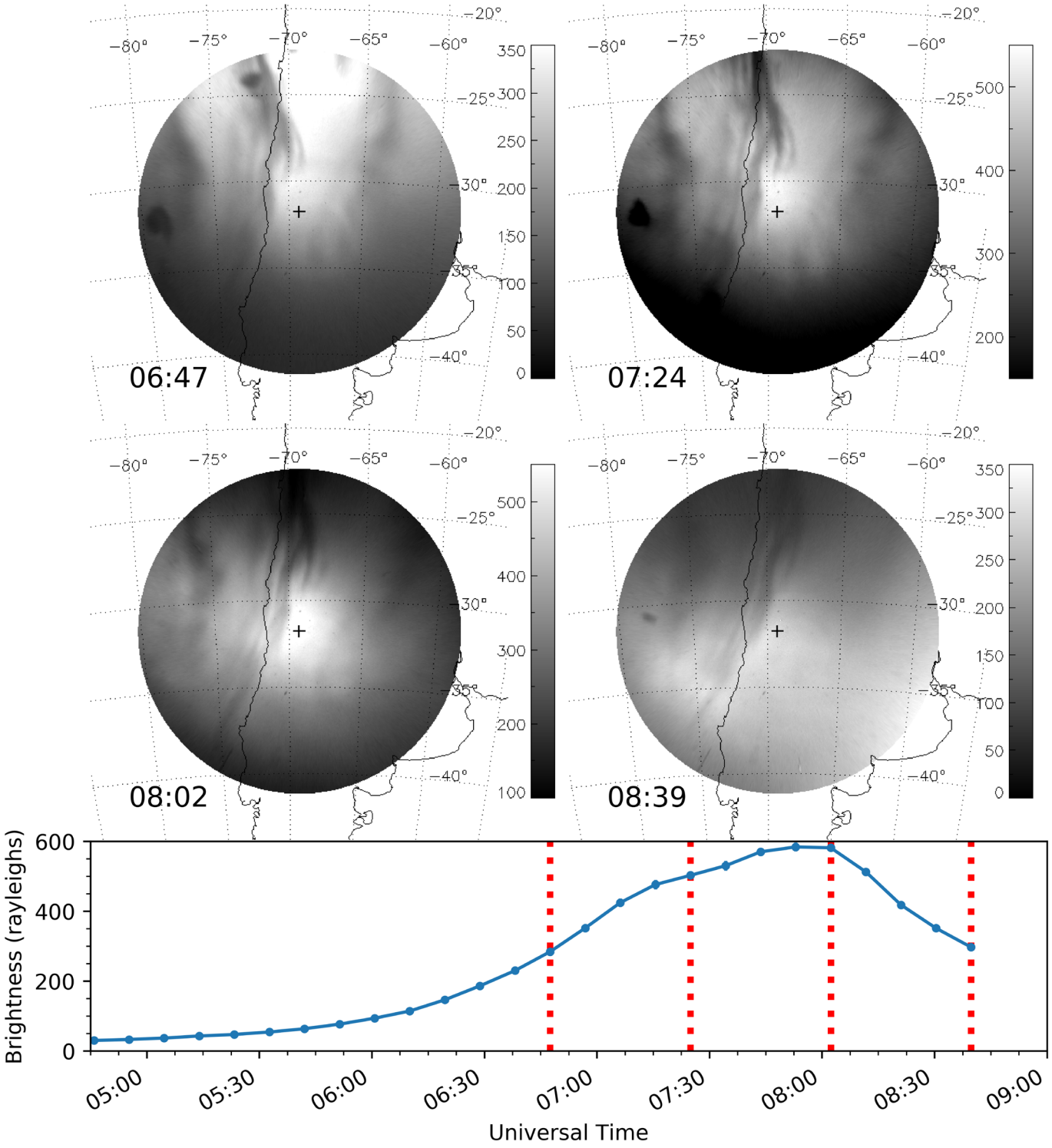

Figure 3. Four unwarped images from the El Leoncito ASI on 29 October 2014 (top). They are unwarped at an altitude of 280 km. The UT of each image is in the lower left corner. Dotted lines indicate latitude and longitude. The gray scale shows the brightness in rayleighs. The scale is different in each image to better show the features. In the earlier images, a BW is visible and can be identified by the increased emission to the North. The airglow depletion due to ESF is seen as the dark feature extending from the top of the image to zenith at about − 72° longitude in the first image. The last image at 08:39 UT is after the BW has passed through zenith. The southern tip of the depletion is in basically the same spot while an eastward motion is observed at lower latitudes. The bottom plot is the brightness in rayleighs at zenith as a function of UT. The brightness wave is the change in brightness that peaks at 08:00 UT. The red dotted lines indicate the times of the images.

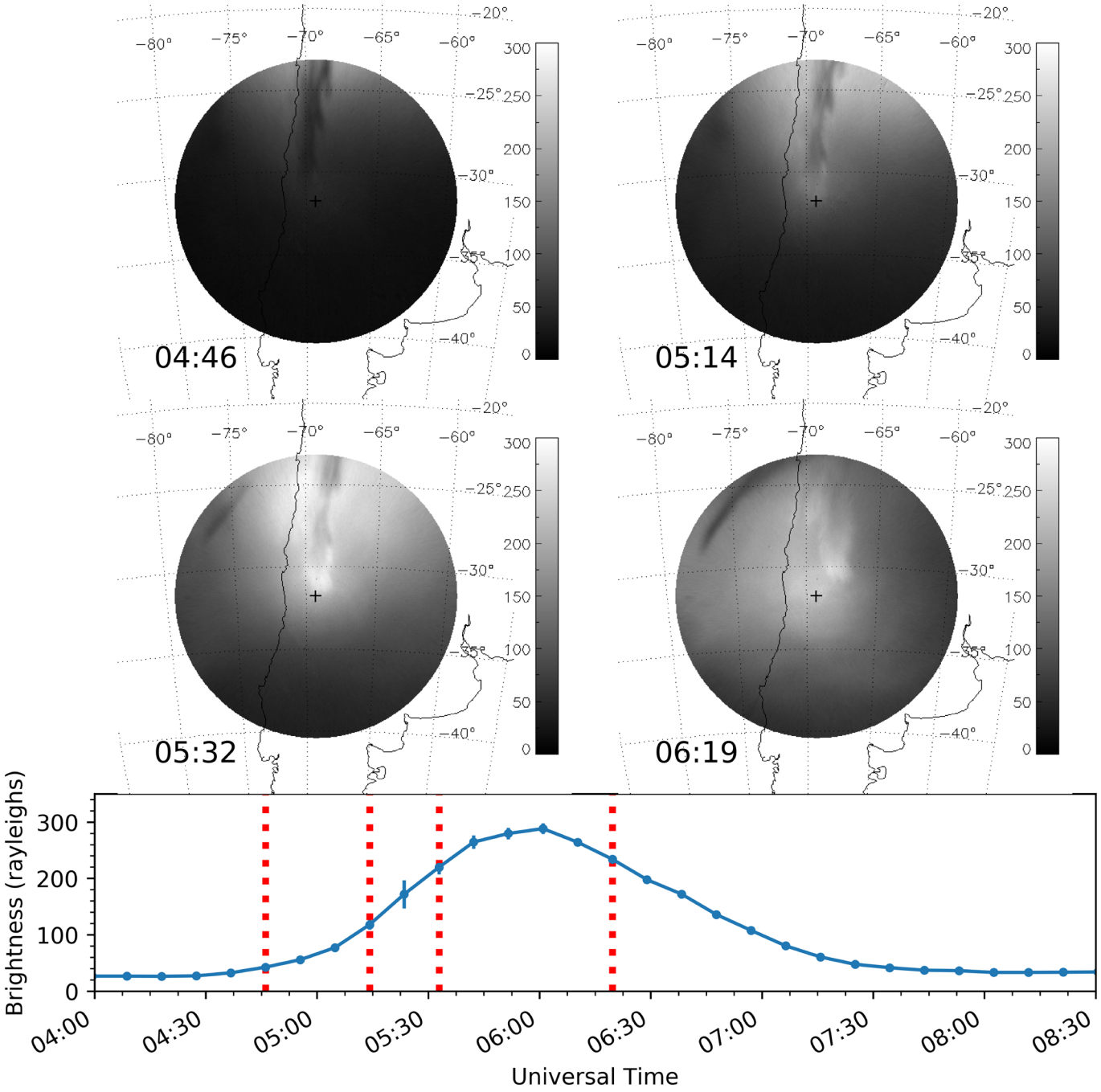

Figure 4. Four unwarped images (top) from the El Leoncito ASI on 13 May 2015. They are unwarped at an altitude of 250 km. The first image is at 04:46 UT. The gray scale shows the brightness in rayleighs. At this time, a BW is just starting to appear in the image and can be identified by the increased emission to the North. The airglow depletion due to ESF is seen as the dark feature extending from the top of the image to zenith at about -70° longitude. The next three images, at 05:14 UT, 05:32 UT, and 06:19 UT, show the progression of the ESF structure as the BW passes through. At 06:19, the ESF structure is no longer an airglow depletion and is now brighter than the background. It extends from the top of the image to about -30° latitude between -70° and -65° longitude. On the bottom is the brightness in rayleighs at zenith as a function of UT. The red lines show the times of the images. The brightness wave is the increase in brightness that peaks at 06:00 UT.

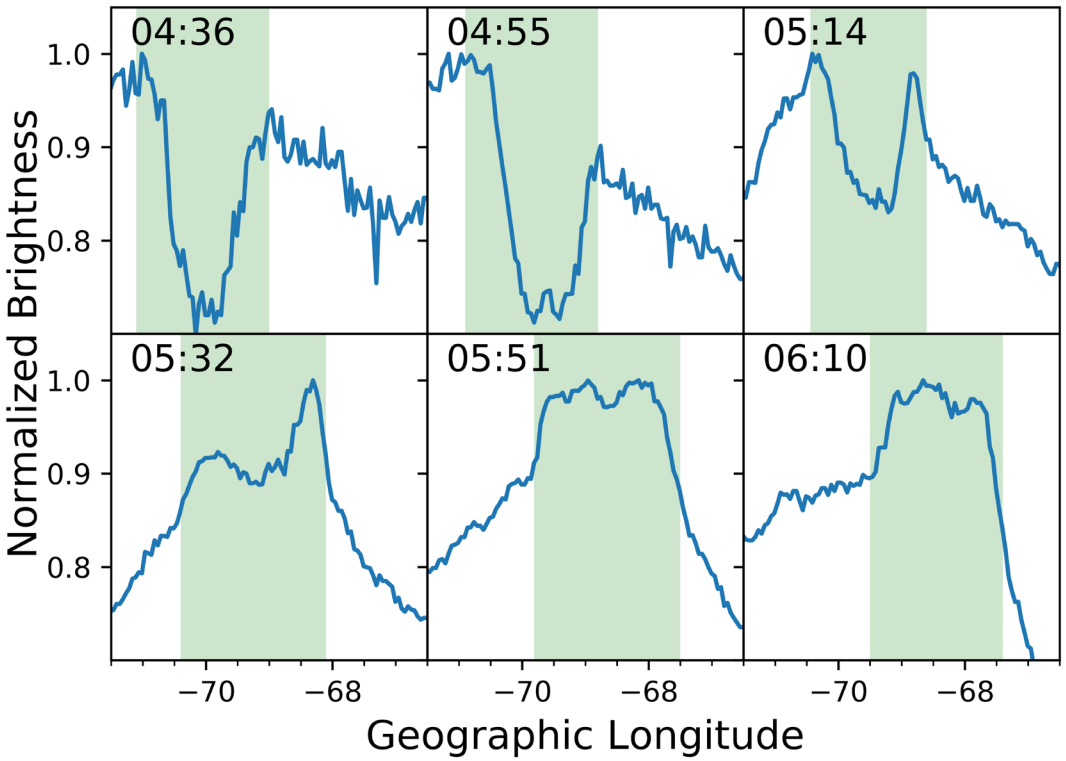

Figure 5. Brightness values at El Leoncito along a constant latitude from -75° to -65° longitude on 13 May 2015. The brightness is a mean of seven pixels centered on 29.5°S. These cuts are from every other 6,300 Å image from this night. The brightness is normalized to the maximum brightness from each cut. Green shading shows the region of interest, highlighting the depletion early in the night and the enhancement later in the night.

date and that changes the airglow alitude calculation. The intensity of 6,300 Å emission calculated as the average from 10 × 10 pixel box at zenith is shown on the bottom. On this night the BW associated with the MTM changes the brightness of the airglow depletion. In the first image of Figure 4 (04:46 UT), the airglow depletion represents a typical example of ESF observed at El Leoncito and the BW is just visible to the north as an increase in brightness. As the BW passes through the region of the depletion, the depletion changes its characteristics and ultimately ends up brighter than the background. The images at 05:14 UT and 05:32 UT show the ESF structure as it evolves. These images show that it is the outer edges of the depletion that brighten first. The last image (06:19 UT) shows the ESF structure after the BW has passed through zenith. The bright region between -70° and -65° longitude and extending south of -30° is the "depletion" that is now brighter than the background. The background is also brighter than the previous image due to the BW. The line plot (bottom) shows the intensity of 6,300 Å emission around the time of the BW, with the brightness increase being the BW. The dotted lines show the times of the images. We also estimated the meridional and zonal velocities of the BW on this night. We estimated the meridional velocity to be about 350 m/s and the zonal velocity to be about 400 m/s. Due to the extended nature of the BW, the error in this estimation is large. The full evolution from a depletion to an enhancement is shown in a movie in the Supporting Information. Although not shown here, 7,774 Å images also exist from this night. A movie of 7,774 Å is included in the Supporting Information; 7,774 Å emission shows the depletion earlier in the night, but during the time that BW occurs in 6,300 Å, the depletion is no longer visible. No BW is observed in 7,774 Å on this night. The 7,774 Å emission is weak on this night so the depletion is most visible when the EIA crest is present and then becomes lost in the noise later in the night. The enhancement is not observed in 7,774 Å.

To show this change in the ESF depletion a more comprehensive manner, we take a cut through the image at 28.49° S and plot brightness versus latitude for six images from this night, as shown in Figure 5. These plots show brightness from 04:36 UT to 06:10 UT. The brightness is normalized in each plot by dividing the data by the maximum value along the cut. Green shading is used to show the depletion as it moves and evolves into an enhancement. In the plots earlier in the night, from 04:36 UT to 05:14 UT, the ESF depletion

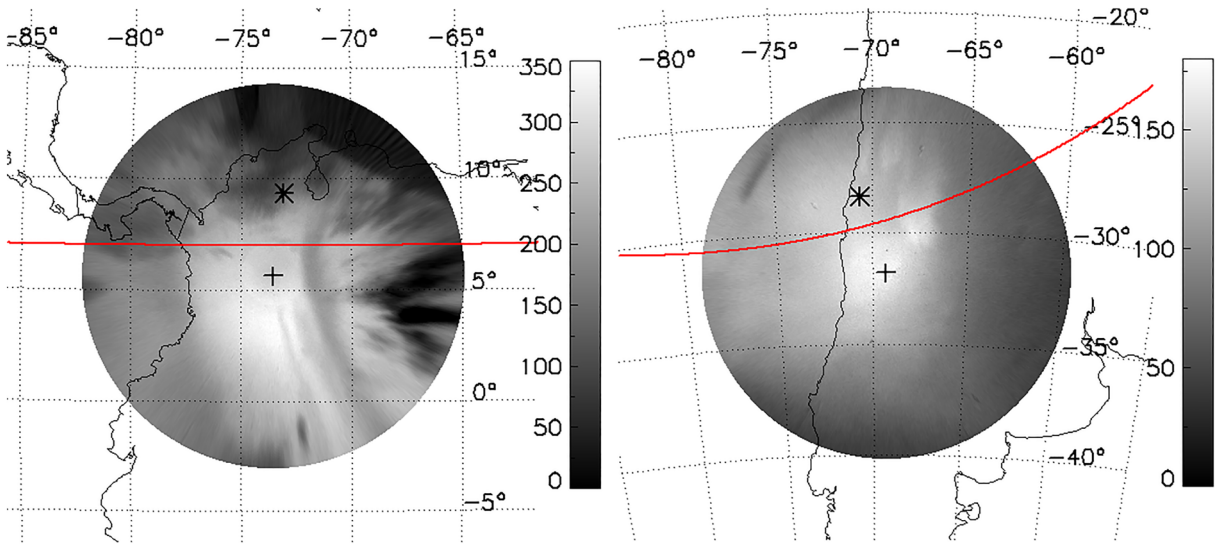

Figure 6. Two unwarped images from 13 May 2015. (Left) An image from Villa de Leyva at 06:40 UT. The red line marks the location where brightness values are extracted for analysis. (Right) An image from El Leoncito at 06:38 UT. The red line is the conjugate line of the line in the Villa de Leyva image. The airglow enhancement between -65° and -70° longitude is the same enhancement from Figure 4 and is conjugate to the depletion between -70° and -75° longitude at Villa de Leyva

is observed as a decrease in brightness. As the brightness wave begins to appear, the overall brightness of the background begins to increase although this is not visible in the normalized brightness. At 05:14, the brightness decrease of the depletion is not as large as in the previous times. At 05:32 UT, the depletion shows a significant change and the eastern edge shows an increase in brightness as it begins to transform into an enhancement. By 05:51 UT, the ESF structure is brighter than the background. Tracking the position of the depletion from each plot to the next shows that the enhancement seen later in the night is the same feature that was a depletion earlier.

On this same night, we also have observations from the Villa de Leyva ASI. There was only a brief period of time where it was clear enough to observe ESF at Villa de Leyva so we are not able to determine if there was a brightness wave. Figure 6 shows an image from Villa de Leyva (06:40 UT) along with a concurrent image from El Leoncito (06:38 UT). The bright airglow enhanced ESF structure is visible during this time in the El Leoncito field of view. In the Villa de Leyva image, an airglow depletion is observed between -70° and -75° longitude, starting at the bottom of the image with the poleward tip extending beyond zenith. This feature is magnetically conjugate to the enhancement in the southern hemisphere. Clouds are observed around the eastern and northern edges of the Villa de Leyva image. To better compare the depletion and enhancement, brightness values along a line of constant latitude at Villa de Leyva, shown as the red line in Figure 6 (left), have been extracted and plotted in blue in Figure 7. The positions of all the points of this line were mapped along magnetic field lines to the opposite hemisphere to measure the conjugate values in the El Leoncito image. The locations of these points are shown as the red curve in Figure 6 (right) and are plotted in green in Figure 7. This plot shows a clear depletion around -72° longitude at Villa de Leyva (blue line). The El Leoncito points have been mapped to the Villa de Leyva field of view so that the two can be directly compared. The green line from El Leoncito shows that there is an airglow enhancement at about -72°, the same place that there is a depletion at Villa de Leyva. This confirms that these two features are conjugate and further shows that there is only an enhancement in one hemisphere.

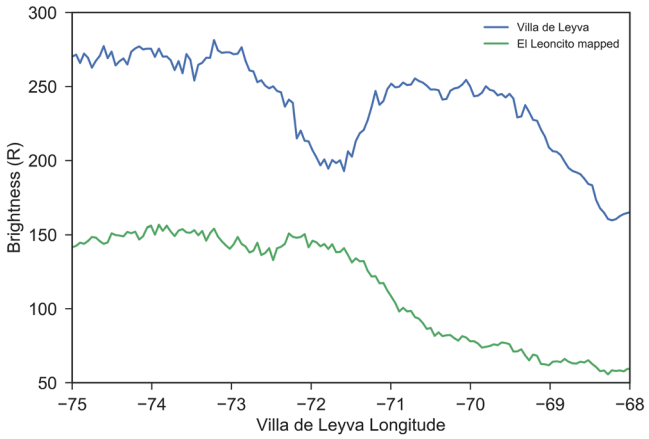

Figure 7. The blue line in this plot shows the brightness values at constant latitude at Villa de Leyva, shown as the red line in Figure 6 (left). The green line shows the brightness values at the conjugate location at El Leoncito, shown as the red line in Figure 6 (right). The El Leoncito positions have been mapped back to the Villa de Leyva longitudes to remove the effects of the Earth's magnetic field.

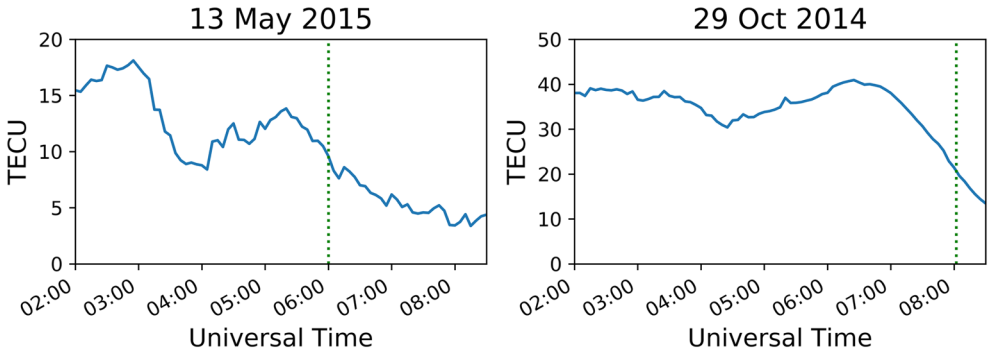

Figure 8. Vertical TEC data from 13 May 2015 and 29 Oct 2014. TEC is calculated by averaging the TEC from a 4° by 4° square. The green dotted line shows the position of the maximum 6,300 Å brightness of the BW on each night. Both nights show an increase in TEC that precedes the BW. 1 TECU is $10^{16} el/m^2$

As discussed earlier, we have also looked at GPS TEC data from the two nights presented in this work. Figure 8 shows vertical TEC from each night at the location of the ASI. TEC is calculated from a variety of receivers in this region and since the GPS satellites are moving, in the 1° bin above the ASI, there is not always a measurement. To account for this, we calculate an average using a 4° by 4° square and this is what is shown in Figure 8. On both nights shown here, there is an increase in TEC. On 29 October 2014, this increase is also observed in 7,774 Å, which is expected since this emission is proportional to TEC. Conversely, no increase in 7,774 Å is observed on 13 May 2015, which may be due to the smaller change in TEC. This increase precedes the BW on both nights. It is not clear whether or not this TEC increase is related to the BW. If it is related to the MTM, it is not obvious why the TEC increase would not happen at the same time as the BW. It could be related to the different heights that are sampled by the TEC measurements compared to the height of the BW. The TEC increase could be related to the thermospheric midnight density maximum, which has been shown to be connected to the MTM (e.g., Akmaev et al., 2010). The MDM lags behind the MTM at the same altitude (Akmaev et al., 2010) so if this TEC increase is related to that then why does it precede the BW? The following night after 13 May 2015 also shows a small BW in 6,300 Å, but on this night, there is no TEC increase. Since the TEC increase is observed on both nights, it seems that there potentially could a connection to the MTM but we do not know what it is and it does not seem to be consistent from night to night. Previous results have investigated nighttime density enhancements in F layer density (Farelo et al., 2002) and in TEC (Olwendo et al., 2012), but none of these papers have connected these enhancements to the MTM. Investigating the connection between these TEC enhancements and the BW is beyond the scope of this paper and we leave this as future work. The TEC measurements do inform us about the motion of the BW. Since the TEC maximum is not concurrent with the BW maximum, the brightness increase must be mostly due to the downward motion of the plasma and not to an overall increase in density. This supports the role of winds in creation of the BW (Colerico et al., 1996, 2006).

4. Discussion

In the previous section, we described a case where an airglow depletion became an airglow enhancement after the passage of a BW associated with the MTM, an effect reported here for the first time. A previous study showed airglow depletions becoming enhancements but without the presence of the BW (Martinis et al., 2009). We use the results from that study to help explain the observations from 13 May 2015 at El Leoncito. Martinis et al. (2009) used an ASI at Arecibo (18.3°N, 66.7°W) and observed nights when a brightening of ESF airglow depletions occurred. Multiple cases were shown, and all of them occurred during December solstice. The enhancements occurred toward the end of the night and no BWs were observed on these nights. The results from Martinis et al. (2009) were the first observations of airglow depletions evolving into airglow enhancements. Krall et al. (2009) provided modeling results to help explain those observations. They used a physics based ionospheric model, the Naval Research Laboratory (NRL) SAMI3 is another model of the ionosphere (SAMI3). With this model they were able to show an airglow depletion evolving into an airglow enhancement in a way that was consistent with the ASI observations. Different background conditions were tested to see what could produce the enhancement. It was found that two factors were important to produce the enhancement in the model. These two factors are the directions of the zonal and meridional winds.

The first requirement for the wind direction is that there must be a convergence of the zonal winds. The zonal winds are what differentiates the enhancement cases from other cases. The converging zonal winds weaken the electric field of the airglow depletion and the weakened electric field decreases upward *ExB* drift within it allowing it to be filled in. The convergence of zonal winds can occur near sunrise when the zonal winds switch directions (Rishbeth, 1971). This is consistent with the observations from Martinis et al. (2009) that show the enhancements at Arecibo late in the night, close to sunrise, so there is likely to be a convergence of the wind during those times.

The second requirement is that the meridional wind must be in a direction such that when the plasma is dragged with it, the plasma moves downward. In the northern hemisphere this means that the meridional wind must be northward. A northward wind will drag the plasma northward but the plasma is also guided by the magnetic field lines so it will move downward. This movement of the plasma downward is what provides the plasma that fills the depletion and turns it into an enhancement. As plasma moves downward, the airglow increases. Thus, at Arecibo the meridional wind must be northward. The climatology over Arecibo indicates that there is typically a northward meridional wind during local winter and often during this time airglow depletions are observed and do not become enhancements. Thus, in the model the converging zonal wind is a key factor needed to alter the depletion and create an enhancement.

Since these wind conditions have been shown to create the airglow enhancement, we now discuss whether these same conditions can be present at El Leoncito when the BW occurs. There are no measurements of the winds within the field of view of the ASI so we must rely on previous works to determine the probable wind directions. Since El Leoncito is in the southern hemisphere, there must be a southward meridional wind to move plasma down the magnetic field lines. The requirement for the converging zonal winds does not change in the southern magnetic hemisphere. Both of these conditions can occur as a result of the MTM. At El Leoncito, the observations presented here show that the BW travels South-West and previous studies have shown that the MTM is known to create or enhance a poleward wind (Harding et al., 2015; Meriwether et al., 2008). It is this poleward wind that moves the plasma and creates the BW. The presence of the BW indicates that there must be a poleward wind as the BW would not appear without it. Thus the requirement of a poleward wind that moves the plasma down to a lower altitude along magnetic field lines is satisfied by the presence of the BW.

Regarding the zonal winds, past observations have shown that the MTM can cause a reversal or abatement in the typically eastward zonal wind (Colerico et al., 2006; Harding et al., 2015; Meriwether et al., 2008). This reversal due to the MTM can cause a convergence of the zonal wind in the same way as the common reversal near sunrise. On both nights we measured the zonal velocity of the ESF structures. On 13 May 2015 the depletion slows down and reaches a minimum zonal velocity close to zero before the passage of the brightness wave. It then increases in velocity after becoming an enhancement. It is possible that this small zonal velocity near the start of the BW is due to converging winds from the MTM/BW. ON 29 October 2014, no minimum velocity is reached before the BW and the velocity is well above zero until the end of the night.

Winds associated with the MTM/BW have been observed enough in previous studies that we can confidently say that there is a poleward meridional wind and there is a good chance that there is a converging zonal wind. The zonal velocity minimum of the depletion near the start of the BW also supports the presence of a converging zonal wind. It may also be possible that a strong meridional wind can overcome the upward drift created by the electric field. The MTM can create stronger meridional winds than those modeled in Krall et al. (2009) and the plasma may be able to move down without a significant weakening of the electric field. Thus, on some nights the MTM can create the correct conditions put forth in Krall et al. (2009) to produce an airglow enhancement.

On 29 October 2014 there is no enhancement of the ESF depletion even though there is a BW. There must be some difference in conditions between the two nights for there to be an enhancement in one case and not in the other. As discussed earlier, the presence of the BW indicates that there is a poleward wind. Although there are no measurements of the winds on either nights, it is possible that there is not a converging zonal wind. The MTM does not always create a reversal of the zonal wind and if there is only a small abatement, then the converging wind may not be present. Since the zonal velocity of the depletion does not approach zero until after the BW, this may provide evidence that there is no converging zonal wind on this night. This variability in the MTM could explain why there is an enhancement on one night and not the other but ultimately we do not know why the enhancement only occurs on 13 May 2015.

As the ESF structure becomes filled in, it may be expected that it should not end up brighter than the background but should be equal to or slightly less bright than the background. This is explained in Krall et al. (2009) and is now briefly summarized here. The fountain affect that creates the equatorial ionization crest also moves plasma within the ESF depletion. The strong electric fields within the bubble leads the crest regions within the ESF structure to exist at a higher altitude than the crests outside the ESF structure. The higher altitude of the crests within the bubble allows them to persist longer since they are not as affected by recombination. This can lead to enhanced regions of plasma that is held at a higher altitude by the *ExB* drift. When this plasma of greater density moves down quickly, at the lower altitude it now has a greater density than the plasma outside of the ESF structure and appears brighter; 7,774 Å images from this night show a depletion early in the night but then it fades and does not become an enhancement. This is consistent with a downward motion of plasma rather than an overall increase in density in the enhancement.

As shown in Figure 7, the enhancement observed at El Leoncito is magnetically conjugate to a depletion at Villa de Leyva. The simulations from Krall et al. (2009) predicted that the enhancements observed at Arecibo would only occur in one hemisphere due to the direction of the meridional winds. A more recent study supported this prediction by showing conjugate airglow and satellite observations (Park et al., 2016). They found a case where a plasma depletion evolved into an enhancement at Arecibo and conjugate observations from El Leoncito and another ASI in Argentina did not show the enhancement. Our results here also show a hemispheric asymmetry as well but the enhancement is attributed to winds from the MTM and BW, not seasonal winds. It may be possible for the enhancement to occur in both hemispheres when the MTM is the driver of the winds.

No BW was observed at Villa de Leyva but due to intermittent cloud cover there is not enough data to determine whether or not one occurred at any point during the night. Throughout much of the night, there were clouds at Villa de Leyva and there are only a few frames that are useful for observations. Additionally, it is not necessarily expected that the BW would occur at the same time at each site. Although Villa de Leyva and El Leoncito are at similar geomagnetic latitudes, they are at different geographic latitudes (5.6° vs. 31.8°). In general, it is expected that the MTM will occur earlier at lower geographic latitudes, so if there was a BW, it may have occurred earlier at Villa de Leyva. Additionally, the MTM tends to occur earlier in local summer (Akmaev et al., 2010; Martinis et al., 2013), which would also affect the relative time of the MTM between the two sites. These seasonal and latitudinal trends only provide an average picture of the MTM as it varies significantly day to day (Akmaev et al., 2010; Martinis et al., 2013) so is difficult to predict how the the MTM will behave on a given night. The MTM occurs on almost every night (Martinis et al., 2013) but the BW is not as prevalent. We do not have information about whether or not there is a BW at Villa de Leyva so we can not say any more beyond that it may be possible for the enhancement to occur there as well.

5. Summary

In this paper, we analyze ASI images from nights when both ESF depletions and a BW are observed at the same time. It does not happen very often that these features occur at the same time. Until now there had been no observations that showed an interaction between these processes. The case from 13 May 2015 showed that the BW changed the ESF depletion and as it passed through the ESF depletion, the ESF structure becomes brighter than the background. Previous modeling results showed that ESF depletions can become enhancements if the correct thermospheric wind conditions are met. These results indicated that a poleward meridional wind and a converging zonal wind can turn an ESF depletion into an enhancement. Both of these wind conditions have previously been shown to be associated with the MTM/BW. Conjugate observations of a depletion confirm that the enhancement in the southern hemisphere is associated with an ESF structure and further validate the modeling results from Krall et al. (2009). Thus, the MTM can create conditions for the brightening of airglow depletions, as was observed on 13 May 2015.

Acknowledgments
Some of this research was performed while the author held an NRC Research Associateship award at the U.S. Naval Research Laboratory. Dustin Hickey's work is supported by the Office of Naval Research. Work done at Boston University was supported by NSF CEDAR Grant 1552301 and NSF AGS Grant 1123222. The authors wish to acknowledge and thank the continuing assistance from the Directors and personnel of the El Leoncito and Villa de Leyva Observatories. Data used in this work are available online (HYPERLINK "http://www.buimaging.com" www.buimaging.com). GPS TEC data products and access through the Madrigal distributed data system are provided to the community (http://www.openmadrigal.org) by the Massachusetts Institute of Technology (MIT) under support from U.S. National Science Foundation Grant AGS-1242204. Data for TEC processing are provided from the following organizations: UNAVCO, Scripps Orbit and Permanent Array Center, Institut Geographique National, France, International GNSS Service, The Crustal Dynamics Data Information System (CDDIS), National Geodetic Survey, Instituto Brasileiro de Geografia e Estatística, RAMSAC CORS of Instituto Geográfico Nacional de la República Argentina, Arecibo Observatory, Low-Latitude Ionospheric Sensor Network (LISN), Topcon Positioning Systems, Inc., Canadian High Arctic Ionospheric Network, Centro di Ricerche Sismologiche, Systéme d'Observation du Niveau des Eaux Littorales (SONEL), RENAG : REseau NAtional GPS permanent, GeoNet–the official source of geological hazard information for New Zealand, GNSS Reference Networks, Finnish Meteorological Institute, and SWEPOS–Sweden. Access to these data is provided by madrigal network (via http://cedar.openmadrigal.org/).

References

Akmaev, R., Wu, F., Fuller-Rowell, T., & Wang, H. (2009). Midnight temperature maximum (MTM) in whole atmosphere model (WAM) simulations. *Geophysical Research Letters*, *36*, L07108. https://doi.org/10.1029/2009GL037759

Akmaev, R., Wu, F., Fuller-Rowell, T., Wang, H., & Iredell, M. (2010). Midnight density and temperature maxima, and thermospheric dynamics in whole atmosphere model simulations. *Journal of Geophysical Research*, *115*, A08326. https://doi.org/10.1029/2010JA015651

Bilitza, D., Altadill, D., Truhlik, V., Shubin, V., Galkin, I., Reinisch, B., & Huang, X. (2017). International Reference Ionosphere 2016: From ionospheric climate to real-time weather predictions. *Space Weather*, *15*, 418–429. https://doi.org/10.1002/2016SW001593

Colerico, M., Mendillo, M., Fesen, C., & Meriwether, J. (2006). Comparative investigations of equatorial electrodynamics and low-to-mid latitude coupling of the thermosphere-ionosphere system. *Annales Geophysicae*, *24*(2), 503–513. https://doi.org/10.5194/angeo-24-503-2006

Colerico, M., Mendillo, M., Nottingham, D., Baumgardner, J., Meriwether, J., Mirick, J., et al. (1996). Coordinated measurements of f region dynamics related to the thermospheric midnight temperature maximum. *Journal of Geophysical Research*, *101*(A12), 26,783–26,793. https://doi.org/10.1029/96JA02337

Farelo, A. F., Herraiz, M., & Mikhailov, A. V. (2002). Global morphology of night-time NmF2 enhancements. *Annales Geophysicae*, *20*(11), 1795–1806. https://doi.org/10.5194/angeo-20-1795-2002

Fejer, B. G., Scherliess, L., & de Paula, E. R. (1999). Effects of the vertical plasma drift velocity on the generation and evolution of equatorial spread F. *Journal of Geophysical Research*, *104*(A9), 19,859–19,869. https://doi.org/10.1029/1999JA900271

Harding, B. J., Makela, J. J., & Meriwether, J. W. (2015). Estimation of mesoscale thermospheric wind structure using a network of interferometers. *Journal of Geophysical Research: Space Physics*, *120*, 3928–3940. https://doi.org/10.1002/2015JA021025

Herrero, F., & Spencer, N. (1982). On the horizontal distribution of the equatorial thermospheric midnight temperature maximum and its seasonal variation. *Geophysical Research Letters*, *9*(10), 1179–1182. https://doi.org/10.1029/GL009i010p01179

Hickey, D. A., Martinis, C. R., Erickson, P. J., Goncharenko, L. P., Meriwether, J. W., Mesquita, R., et al. (2014). New radar observations of temporal and spatial dynamics of the midnight temperature maximum at low latitude and midlatitude. *Journal of Geophysical Research: Space Physics*, *119*, 10–499. https://doi.org/10.1002/2014JA020719

Hickey, D. A., Martinis, C. R., Mendillo, M., Baumgardner, J., Wroten, J., & Milla, M. (2018). Simultaneous 6300 Å airglow and radar observations of ionospheric irregularities and dynamics at the geomagnetic equator. *Annales Geophysicae*, *36*(2), 473–487. https://doi.org/10.5194/angeo-36-473-2018

Hysell, D. (2000). An overview and synthesis of plasma irregularities in equatorial spread f. *Journal of Atmospheric and Solar-Terrestrial Physics*, *62*(12), 1037–1056. https://doi.org/10.1016/S1364-6826(00)00095-X

Kelley, M. C., & Maruyama, T. (1992). A diagnostic model for equatorial spread F 2. The effect of magnetic activity. *Journal of Geophysical Research*, *97*(A2), 1271–1277. https://doi.org/10.1029/91JA02607

Keskinen, M., Ossakow, S., Basu, S., & Sultan, P. (1998). Magnetic-flux-tube-integrated evolution of equatorial ionospheric plasma bubbles. *Journal of Geophysical Research*, *103*(A3), 3957–3967. https://doi.org/10.1029/97JA02192

Krall, J., Huba, J., & Martinis, C. (2009). Three-dimensional modeling of equatorial spread F airglow enhancements. *Geophysical Research Letters*, *36*, L10103. https://doi.org/10.1029/2009GL038441

Krall, J., Huba, J. D., Ossakow, S. L., & Joyce, G. (2010). Equatorial spread F fossil plumes. *Annales Geophysicae*, *28*(11), 2059–2069. https://doi.org/10.5194/angeo-28-2059-2010

Martinis, C., Baumgardner, J., Mendillo, M., Su, S.-Y., & Aponte, N. (2009). Brightening of 630.0 nm equatorial spread-F airglow depletions. *Journal of Geophysical Research*, *114*, A06318. https://doi.org/10.1029/2008JA013931

Martinis, C., Baumgardner, J., Wroten, J., & Mendillo, M. (2018). All-sky-imaging capabilities for ionospheric space weather research using geomagnetic conjugate point observing sites. *Advances in Space Research*, *61*(7), 1636–1651. https://doi.org/10.1016/j.asr.2017.07.021

Martinis, C., Hickey, D., Oliver, W., Aponte, N., Brum, C., Akmaev, R., et al. (2013). The midnight temperature maximum from Arecibo incoherent scatter radar ion temperature measurements. *Journal of Atmospheric and Solar-Terrestrial Physics*, *103*, 129–137. https://doi.org/10.1016/j.jastp.2013.04.014

Martinis, C. R., Mendillo, M. J., & Aarons, J. (2005). Toward a synthesis of equatorial spread F onset and suppression during geomagnetic storms. *Journal of Geophysical Research*, *110*, A07306. https://doi.org/10.1029/2003JA010362

Mendillo, M., & Baumgardner, J. (1982). Airglow characteristics of equatorial plasma depletions. *Journal of Geophysical Research*, *87*(A9), 7641–7652. https://doi.org/10.1029/JA087iA09p07641

Meriwether, J., Faivre, M., Fesen, C., Sherwood, P., & Veliz, O. (2008). New results on equatorial thermospheric winds and the midnight temperature maximum. *Annales Geophysicae*, *26*(3), 447–466. https://doi.org/10.5194/angeo-26-447-2008

Olwendo, O. J., Baki, P., Mito, C., & Doherty, P. (2012). Characterization of ionospheric GPS total electron content (gpstec) in low latitude zone over the Kenyan region during a very low solar activity phase. *Journal of Atmospheric and Solar-Terrestrial Physics*, *84-85*, 52–61. https://doi.org/10.1016/j.jastp.2012.06.003

Otsuka, Y., Kadota, T., Shiokawa, K., Ogawa, T., Kawamura, S., Fukao, S., & Zhang, S.-R. (2003). Optical and radio measurements of a 630-nm airglow enhancement over Japan on 9 September 1999. *Journal of Geophysical Research: Space Physics*, *108*(A6), 1252. https://doi.org/10.1029/2002JA009594

Park, J., Martinis, C. R., Lhr, H., Pfaff, R. F., & Kwak, Y.-S. (2016). Hemispheric asymmetry in transition from equatorial plasma bubble to blob as deduced from 630.0 nm airglow observations at low latitudes. *Journal of Geophysical Research: Space Physics*, *121*, 881–893. https://doi.org/10.1002/2015JA022175

Picone, J., Hedin, A., Drob, D. P., & Aikin, A. (2002). NRLMSISE-00 empirical model of the atmosphere: Statistical comparisons and scientific issues. *Journal of Geophysical Research*, *107*(A12), 1468. https://doi.org/10.1029/2002JA009430

Rideout, W., & Coster, A. (2006). Automated GPS processing for global total electron content data. *GPS solutions*, *10*(3), 219–228.

Rishbeth, H. (1971). Polarization fields produced by winds in the equatorial F-region. *Planetary and Space Science*, *19*(3), 357–369. https://doi.org/10.1016/0032-0633(71)90098-5

Rodrigues, F. S., Hickey, D. A., Zhan, W., Martinis, C. R., Fejer, B. G., Milla, M. A., & Arratia, J. F. (2018). Multi-instrumented observations of the equatorial F-region during june solstice: Large-scale wave structures and spread-F. *Progress in Earth and Planetary Science*, *5*(1), 14. https://doi.org/10.1186/s40645-018-0170-0

Sultan, P. (1996). Linear theory and modeling of the Rayleigh-Taylor instability leading to the occurrence of equatorial spread F. *Journal of Geophysical Research*, *101*(A12), 26,875–26,891. https://doi.org/10.1029/96JA00682

Vierinen, J., Coster, A. J., Rideout, W. C., Erickson, P. J., &Norberg, J. (2015). Statistical framework for estimating GNSS bias. *Atmospheric Measurement Techniques*. https://doi.org/10.5194/amtd-8-9373-2015

Weber, E., Basu, S., Bullett, T., Valladares, C., Bishop, G., Groves, K., et al. (1996). Equatorial plasma depletion precursor signatures and onset observed at 11 south of the magnetic equator. *Journal of Geophysical Research*, *101*(A12), 26,829–26,838. https://doi.org/10.1029/96JA00440

Weber, E., Buchau, J., Eather, R., & Mende, S. (1978). North-south aligned equatorial airglow depletions. *Journal of Geophysical Research*, *83*(A2), 712–716. https://doi.org/10.1029/JA083iA02p00712

Woodman, R. F., & La Hoz, C. (1976). Radar observations of F region equatorial irregularities. *Journal of Geophysical Research*, *81*(31), 5447–5466. https://doi.org/10.1029/JA081i031p05447

Zhan, W., Rodrigues, F. S., & Milla, M. A. (2018). On the genesis of postmidnight equatorial spread F: Results for the american/peruvian sector. *Geophysical Research Letters*, *45*, 7354–7361. https://doi.org/10.1029/2018GL078822